Zhang, Y., Wang, R., Zschau, J., Chen, Y.-t., Parolai, S., Dahm, T. (2014): Automatic imaging of earthquake rupture processes by iterative deconvolution and stacking of high-rate GPS and strong motion seismograms. - *Journal of Geophysical Research*, *119*, 7, p. 5633-5650.

DOI: http://doi.org/10.1002/2013JB010469

AGU PUBLICATIONS

JGR

Journal of Geophysical Research: Solid Earth

RESEARCH ARTICLE
10.1002/2013JB010469

Key Points:
- Robust method for automatic imaging of earthquake source
- Near-real-time source inversion using near-field GPS and strong motion networks
- Tsunami early warning and earthquake rapid response

Supporting Information:
- Readme
- Supplementary Text

Correspondence to:
R. Wang,
wang@gfz-potsdam.de

Citation:
Zhang, Y., R. Wang, J. Zschau, Y.-t. Chen, S. Parolai, and T. Dahm (2014), Automatic imaging of earthquake rupture processes by iterative deconvolution and stacking of high-rate GPS and strong motion seismograms, *J. Geophys. Res. Solid Earth*, *119*, 5633–5650, doi:10.1002/2013JB010469.

Received 26 JUN 2013
Accepted 19 JUN 2014
Accepted article online 25 JUN 2014
Published online 10 JUL 2014

Automatic imaging of earthquake rupture processes by iterative deconvolution and stacking of high-rate GPS and strong motion seismograms

Yong Zhang[1,2], Rongjiang Wang[2], Jochen Zschau[2], Yun-tai Chen[1,3], Stefano Parolai[2], and Torsten Dahm[2]

[1]School of Earth and Space Sciences, Peking University, Beijing, China, [2]Helmholtz Centre Potsdam, GFZ German Research Centre for Geosciences, Potsdam, Germany, [3]Institute of Geophysics, China Earthquake Administration, Beijing, China

Abstract By combining the complementary advantages of conventional network inversion and backprojection methods, we have developed an iterative deconvolution and stacking (IDS) approach for imaging earthquake rupture processes with near-field complete waveform data. This new approach does not need any manual adjustment of the physical (empirical) constraints, such as restricting the rupture time and duration, and smoothing the spatiotemporal slip distribution. Therefore, it has the ability to image complex multiple ruptures automatically. The advantages of the IDS method over traditional linear or nonlinear optimization algorithms are demonstrated by the case studies of the 2008 Wenchuan and 2011 Tohoku earthquakes. For such large earthquakes, the IDS method is considerably more stable and efficient than previous inversion methods. Additionally, the robustness of this method is demonstrated by comprehensive synthetic tests, indicating its potential contribution to tsunami and earthquake early warning and rapid response systems. It is also shown that the IDS method can be used for teleseismic waveform inversions. For the two major earthquakes discussed here, the IDS method can provide, without tuning any physical or empirical constraints, teleseismic rupture models consistent with those derived from the near-field GPS and strong motion data.

1. Introduction

In recent decades, seismologists have expended great efforts in developing methods for the rapid determination of earthquake source parameters, which include the hypocenter, the origin time, the magnitude, the moment tensor and/or focal mechanism, and the kinematic rupture process. Nowadays, the estimation of the hypocenter and magnitude has become an automated routine of seismological agencies around the world. Some institutions, such as the United States Geological Survey (USGS), the Global Centroid Moment Tensor (GCMT) group [*Ekström et al.*, 2012], and the German Research Centre for Geosciences, can release their automatic (sometimes manually revised) moment tensor solutions within 1 h to several hours. For the rapid response of earthquake emergency and/or earthquake early warning (EEW), however, hypocentral location, magnitude, and moment tensor solution are still not enough to describe all source characteristics, since they cannot offer the slip distribution and the rupture kinematics, which are important for simulating strong ground motion and/or tsunami waves. Therefore, the timely identification of all of these rupture characteristics is one of the most essential requirements for EEW [*Allen et al.*, 2009]. If information about the spatiotemporal evolution of the rupture is available soon after an event's occurrence, intensities and/or tsunami heights can then be predicted for rapid response.

Currently, there are two most commonly used methods for imaging the rupture process: the conventional network inversion and the backprojection. In the past, these methods have significantly improved our knowledge of earthquake ruptures and their complexities. The conventional network inversion method can use both near-field and teleseismic waveform data [e.g., *Kikuchi and Kanamori*, 1982; *Olson and Apsel*, 1982; *Hartzell and Heaton*, 1983; *Ji et al.*, 2002; *Sekiguchi and Iwata*, 2002; *Yagi et al.*, 2004; *Vallée*, 2004]. The various algorithms of the conventional network inversion can be classified into linear and nonlinear types. The only difference lies in the parameterization of the source time function (STF) of the subfaults. In linear methods, the subfault source time function is also discretized. Normally it is expressed by multiple triangles, equidistantly distributed within a presumed time window [*Sekiguchi and Iwata*, 2002; *Yagi et al.*, 2004]. The unknowns are the scaling factors of the triangles, which are related linearly to the data. In contrast, nonlinear methods use a preselected elementary source time function (ESTF) for each subfault. Usually, the ESTF is

simplified by a single triangular function. In recent years, there have been studies that consider dynamically consistent ESTFs, but they are more commonly used for forward modeling strong ground motion [*Pitarka et al.*, 2000; *Guatteri et al.*, 2003; *Tinti et al.*, 2005; *Liu et al.*, 2006; *Graves and Pitarka*, 2010], with a few applications for finite-fault inversion [*Ji et al.*, 2002; *Wei et al.*, 2013]. In general, all ESTFs are defined with three free parameters: amplitude, rupture time, and risetime, all of which can be subfault dependent. In particular, the latter two need to be searched for through a nonlinear approach, such as by the use of the simulated annealing [*Hartzell and Liu*, 1996; *Ji et al.*, 2002]. To achieve a stable and physically reasonable solution, a priori knowledge and additional empirical constraints at the expense of a degree of data fit are necessary in both linear and nonlinear algorithms, for example, restricting the variation range of the rupture velocity and smoothing the spatial-temporal rupture distribution. The weights of these constraints, which determine the compromise among the data fit, the source resolution, and the solution stability, often need to be optimized manually. The strong influence of these constraints on the inversion results makes it difficult to fully automatize the conventional inversion methods and therefore reduces their application potential in early warning and rapid response systems.

The backprojection method is based on the phase interference principle [e.g., *Ishii et al.*, 2005; *Krüger and Ohrnberger*, 2005]. Generally, it uses single-wave phase data, mostly the direct *P* waves recorded by a teleseismic seismometer array of limited aperture. Recently, there have been a few studies successfully applying backprojection to high-frequency *S* waves recorded by strong motion networks [*Allmann and Shearer*, 2007; *Honda and Aoi*, 2009; *Honda et al.*, 2008, 2011]. In contrast to the conventional network inversion, backprojection works with fewer free parameters and, in particular, does not need Green's functions. On the other hand, however, the coherency stacking technique used in the backprojection approach does not allow one to retrieve actual slip or slip rate values, but just a relative measure of radiation strength in the frequency band of interest.

In this study, we present a new approach which benefits from the complementary advantages of the conventional network inversion and backprojection methods. To serve in earthquake rapid response and tsunami early warning, the new approach should be robust and efficient so that it can be implemented for the automatic analysis of strong motion and high-rate GPS data. After an introduction to the basic theory and the technical details of the new approach, we will demonstrate the value of the new method using synthetic tests and case studies, namely, for the 2008 Wenchuan and 2011 Tohoku earthquakes. Finally, we will discuss the potential contribution of the new approach to tsunami and earthquake early warning and rapid response systems.

2. Method

In the backprojection approach, seismic records from different stations are stacked after applying appropriate time shifts that depend on their distances to a target subfault. The time shifting is in principle comparable with tuning a satellite antenna. There are two limitations for the backprojection approach. One is that the spatial extent of the seismic network (the antenna aperture) should be much smaller than the distance to the earthquake source so that the seismic signals propagate through about the same path from the source to the network and therefore have coherent waveforms. The second limitation is that the approach can only use a single phase of seismic waves (mostly the direct *P* waves), because the overlapping of different seismic phases may make the received seismic records incoherent, even within a small network. Because of these two limitations, the backprojection approach is mostly applied to a local or regional seismic array at teleseismic distances (30°–90° for direct *P* waves).

To extend the backprojection technique so that it can work for complete waveform data with arbitrary spatial coverage and also in the low-frequency band, we propose correcting the path and radiation effects by using synthetic (or empirical, if available) Green's functions. Instead of stacking the seismic records directly, we stack apparent source time functions (ASTFs) observed at different stations. The ASTFs of a selected subfault can be obtained by deconvolving its Green's functions from the observed seismograms. For each observation site, the ASTF of the selected subfault consists in principle of two pieces of information. One is the true source signal from this subfault and the other is the aliasing signal induced from the remaining subfaults. The former is coherent and in phase for all stations, but the latter is generally incoherent and in different phases for different stations. Through the stacking, the true source signal will be amplified, and the aliasing signals will be mostly canceled by each other. At this step, the new method works in a similar way to the backprojection approach. Note that the presented scheme differs from how the ASTF deconvolution has been carried out, in many previous studies, e.g., *Mori and Hartzell* [1990], *Dreger* [1994], *Velasco et al.* [1994], and *Chen and Xu* [2000],

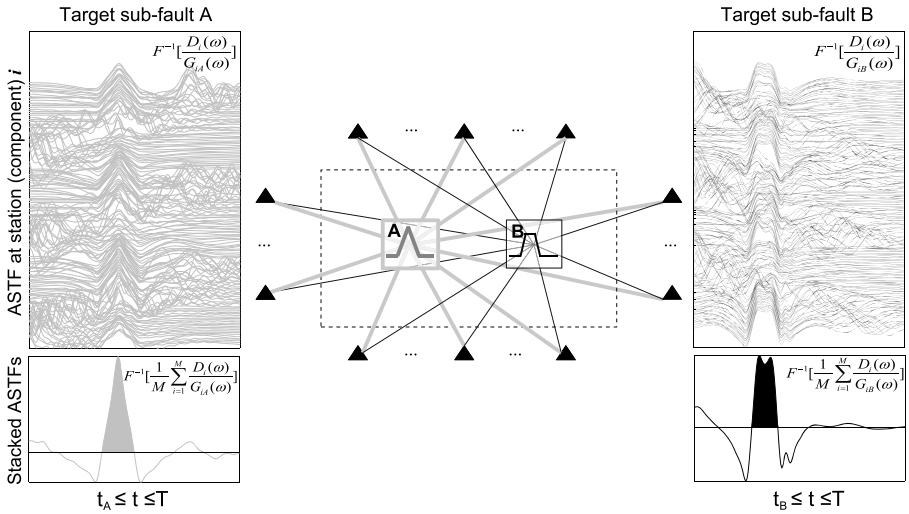

Figure 1. Description of the principle behind the deconvolution and stacking approach. In the input model, two subfaults (left) A and (right) B within a potential fault are ruptured, whose (middle) STFs are described by a triangle and a trapezoid, respectively. Synthetic waveform data (velocity seismograms) are generated for a network of observation sites (black triangles) around the potential fault (dashed rectangle). The network coverage relative to the fault is designed to be comparable with the case of the 2011 Tohoku earthquake (see Figure 5). (left and right) The comparisons of the ASTFs and their stacked results for the target subfaults A and B, respectively. Parameters t_A and t_B are the earliest possible rupture times of subfaults A and B, respectively, and T is the preestimated time window. For each subfault, the maximum positive wavelet (shadowed part) of the stacked ASTF is used as the inferred STF in the IDS method presented in this study.

where the earthquake is approximated by a point source. In those previous studies, by stacking the ASTFs, one can obtain a rough estimate of the STF for the whole earthquake without considering spatial rupture variability [*Xu et al.*, 2002]. In this study, however, we stack the ASTFs for each subfault aiming to retrieve the subfault STF.

Figure 1 shows a simple synthetic test which describes how the new method works. The input source model includes two ruptured subfaults (A and B), whose STFs are described by a triangle and a trapezoid, respectively (Figure 1, middle). Synthetic data (velocity seismograms) are generated for a network of observation sites around the assumed fault. The network coverage relative to the fault is designed to be comparable with the case of the 2011 Tohoku earthquake. For any location on the fault plane, the local ASTFs are calculated by deconvolving the data with the synthetic Green's function based on the focal mechanisms of strike = 193°, dip = 14°, and rake = 81°, released by USGS (http://comcat.cr.usgs.gov/earthquakes/eventpage/pde20110311054624120_29#scientific). The results show that almost all the ASTFs for each subfault exhibit a coherent signature of their own input STF and some incoherent noise induced by the other subfault STFs. After stacking the ASTFs, the incoherent noise becomes vanishingly small, while the coherent part is amplified, leading to an inferred STF close to the true one. Through this deconvolution and stacking approach, the whole potential rupture area can be scanned patch by patch. When the subfault STFs are detected, their contributions to the observed data are estimated through forward modeling and then removed from the data. Usually, the procedure is repeated until the cumulative seismic moment converges or the misfit between the data and the synthetics cannot be further reduced. In this sense, the new method may be called the iterative deconvolution and stacking (IDS) method. In the following, we will outline the theory and the developed algorithm of this IDS method.

We define $d_i(t)$ as the data from an observation site (station) i ($i = 1, 2, \ldots, M$), $s_j(t)$ as the STF (slip rate time history) of subfault ($j = 1, 2, \ldots, N$), and $g_{ij}(t)$ as the Green's function, i.e., the synthetic data at station i caused by a delta slip rate impulse at subfault j, where t ($0 \le t \le T$) is the time since the earthquake's occurrence. The observation equations then read as

$$d_i(t) = \sum_j^N \int_0^t g_{ij}(t-\tau)\dot{s}_j(\tau)d\tau, \quad (i = 1, 2, \ldots, M). \tag{1}$$

If the Fourier spectra of $d_i(t)$, $\dot{s}_j(t)$, and $g_{ij}(t)$ are denoted by $D_i(\omega)$, $S_j(\omega)$, and $G_{ij}(\omega)$, respectively, the frequency domain observation equations then read as

$$D_i(\omega) = \sum_{j=1}^{N} \left[G_{ij}(\omega) S_j(\omega) \right], \quad (i = 1, 2, \ldots, M), \tag{2}$$

where ω is the angular frequency.

For any selected subfault J, we may stack the ASTFs observed at all the stations and obtain

$$\frac{1}{M} \sum_{i=1}^{M} \frac{D_i(\omega)}{G_{iJ}(\omega)} = S_J(\omega) + \frac{1}{M} \sum_{i=1}^{M} \sum_{j \neq J}^{N} \frac{G_{ij}(\omega) S_j(\omega)}{G_{iJ}(\omega)}. \tag{3}$$

The results obtained after stacking include two pieces of information. The first is the STF of subfault J, which is what we want to extract. The second is the disturbance caused by other subfault STFs, which can be rewritten in the form

$$\Delta_J(\omega) = \frac{1}{M} \sum_{j \neq J}^{N} S_j(\omega) \sum_{i=1}^{M} \frac{G_{ij}(\omega)}{G_{iJ}(\omega)}. \tag{4}$$

In the case of an ideal network coverage around the fault, $G_{ij, j \neq J}$ is on average incoherent with G_{iJ}. Thus, we suppose that Δ_J can be negligible compared to S_J and suggest the approximation

$$S_J(\omega) \approx \frac{1}{M} \sum_{i=1}^{M} \frac{D_i(\omega)}{G_{iJ}(\omega)}. \tag{5}$$

Equation (5) means that we can obtain an approximation of each subfault's STF by stacking the deconvolved seismograms. In practice, the deconvolution given in equation (5) can be stabilized by using the so-called water level approach [*Helmberger and Wiggins*, 1971],

$$S_J(\omega) \approx \frac{1}{M} \sum_{i=1}^{M} \frac{D_i(\omega) G_{iJ}^{*}(\omega)}{\max\left(|G_{iJ}(\omega)|^2, |G_{iJ}(\omega)|^2_{\max} \cdot \varepsilon^2 \right)}, \tag{6}$$

where G_{iJ}^{*} is the complex conjugate of G_{iJ} and ε is the dimensionless water level parameter. The time domain STFs (slip rate time history) are obtained by the inverse Fourier transform,

$$\dot{s}_J(t) = F^{-1}[S_J(\omega)]. \tag{7}$$

To ensure stability, we choose ε in equation (6) to be as large as 0.1. The large water level is helpful for minimizing disturbances in imaging the rupture propagation, because it leads to only the most significant rupture signals being retrieved. On the other hand, a complex rupture process that involves temporally discrete episodes of rupture on the same fault patch cannot be retrieved through a single deconvolution and stacking process. Therefore, the deconvolution and stacking procedures normally need to be performed iteratively. Additionally, to minimize artifacts from large oscillatory ASTFs for stations (components) close to the theoretical nodal planes, the STF estimated using equation (7) needs to be examined based on sensitivity tests. For these reasons outlined above, we suggest the following pseudo algorithm:

1. *Discretization*. Discretize the potential rupture area into a number of subfaults identified by $j = 1, 2, \ldots, N$, each of which is represented by a point source (so far with uniform source mechanisms).
2. *Deconvolution*. Calculate the ASTFs for each subfault by deconvolving the current residual data with synthetic Green's functions (with known focal mechanism). The current residual data are denoted by $\Delta d_i(t)$ [$=d_i(t)$ in the first iteration] for all observation sites $i = 1, 2, \ldots, M$.
3. *Stacking*. Stack the ASTFs of all the stations for each subfault and select the maximum positive wavelet (see Figure 1) as an incremental STF $\Delta \dot{s}_j(t)$ for the concerned subfault in the current iteration.
4. *Scaling*. Scale all the incremental STFs separately, $\Delta \dot{s}_j(t) \Rightarrow A_j \Delta \dot{s}_j(t)$, so that the synthetic data associated with each other best fit the current residual data. In the least squares sense, A_j is calculated by

$$A_j = \frac{\sum_{i=1}^{M} \int_0^T \Delta d_i(t) \Delta y_{ij}(t) dt}{\sum_{i=1}^{M} \int_0^T \left[\Delta y_{ij}(t) \right]^2 dt}, \tag{8}$$

where $\Delta y_{ij}(t)$ is the incremental synthetic data at station i produced by $\Delta \dot{s}_j(t)$,

$$\Delta y_{ij}(t) = \int_0^t g_{ij}(t-\tau)\Delta \dot{s}_j(\tau)d\tau. \tag{9}$$

Negative A_j values need to be set to zero (positivity constraint). After $\Delta \dot{s}_j(t)$ has been scaled, the updated $\Delta y_{ij}(t)$ has the property that

$$\sum_{i=1}^{M}\int_0^T\left[\Delta y_{ij}(t)\right]^2 dt = \sum_{i=1}^{M}\int_0^T \Delta d_i(t)\Delta y_{ij}(t)dt. \tag{10}$$

5. *Regularization*. Modify $\Delta \dot{s}_j(t)$ with a sensitivity factor $f_j \propto R_j^2\gamma_j$, where R_j^2 is the relative data fit of $\Delta \dot{s}_j(t)$ to $\Delta d_i(t)$,

$$R_j^2 = 1 - \frac{\sum_{i=1}^{M}\int_0^T\left[\Delta d_i(t) - \Delta y_{ij}(t)\right]^2 dt}{\sum_{i=1}^{M}\int_0^T[\Delta d_i(t)]^2 dt}, \tag{11}$$

and γ_j is the correlation coefficient between $\Delta y_{ij}(t)$ and the original data $d_i(t)$,

$$\gamma_j = \frac{\sum_{i=1}^{M}\int_0^T d_i(t)\Delta y_{ij}(t)dt}{\sqrt{\sum_{i=1}^{M}\int_0^T[d_i(t)]^2 dt}\sqrt{\sum_{i=1}^{M}\int_0^T\left[\Delta y_{ij}(t)\right]^2 dt}}. \tag{12}$$

Negative f_j values also need to be set to zero (again the positivity constraint). Note that by using equation (10), it can be easily proved that R_j^2 is equal to the squared correlation coefficient between $\Delta y_{ij}(t)$ and $\Delta d_i(t)$. Thus, R_j^2 is also called the coefficient of determination.

6. *Smoothing*. In the first iteration, calculate the cumulative slip $\Delta s_j = \int_0^T \Delta \dot{s}_j(t)dt$ $(j = 1, 2, \ldots, N)$, find the largest asperity (the one including the peak slip value, max(Δs_j)), and determine the azimuthally averaged and normalized height-distance curve $h_o(r)$ for the slip within this asperity, where r is the distance to the peak slip. Parameter $h_o(r)$ will be used as a reference for the characteristic slip roughness. In all the following iterations, the obtained Δs_j are examined for their characteristic roughness, $h(r)$. If $h(r)$ is below $h_o(r)$, i.e., indicates a larger roughness, a space domain low-pass filter (e.g., via a 2-D moving average window) is applied to $\Delta \dot{s}_j(t)$ repeatedly until the resulted $h(r)$ best fits $h_o(r)$.
7. *Re-scaling*. Re-scale $\Delta \dot{s}_j(t)$ globally with a uniform scaling factor A, which is determined so that the synthetic data associated with all $\Delta \dot{s}_j(t)$ collectively best fit the current residual data. Add them to the cumulative STFs $\dot{s}_j(t)$ and then update the residual data for the next iteration. The global scaling factor A is calculated by

$$A = \frac{\sum_{i=1}^{M}\int_0^T \Delta d_i(t)\sum_{j=1}^{N}\Delta y_{ij}(t)dt}{\sum_{i=1}^{M}\int_0^T\left[\sum_{j=1}^{N}\Delta y_{ij}(t)\right]^2 dt}. \tag{13}$$

8. *Iteration*. Repeat steps 2–7 until the misfit between the cumulative synthetic data and the original data cannot be further reduced, where the misfit function is defined by the ratio of unfitted observed waves compared to the complete observed waves in the least squares sense, i.e., $\sigma^2 = \frac{\sum_{i=1}^{M}\int_0^T\left[d_i(t) - \sum_{j=1}^{N} y_{ij}(t)\right]^2 dt}{\sum_{i=1}^{M}\int_0^T[d_i(t)]^2 dt}$.
Practically, it is thought to be excellent for the relative misfit values between 0 and 0.2, good for 0.2–0.4, acceptable for 0.4–0.6, and unsatisfactory above 0.6.

Note that steps 5 and 6 are both necessary. Step 5 is the sensitivity-based regularization. By using this step, possible overestimation can be prevented for subfaults located too far from the network or at the sites, which are poorly resolved by the network. For these subfaults, the amplitudes of the Green's functions are relatively small so that the deconvolution results (i.e., the ASTFs) may include large artifacts. We recall that in the classic singular-value decomposition method, the regularization is solved by excluding the eigenvectors associated with zero or very small eigenvalues, while in the conventional inversion methods,

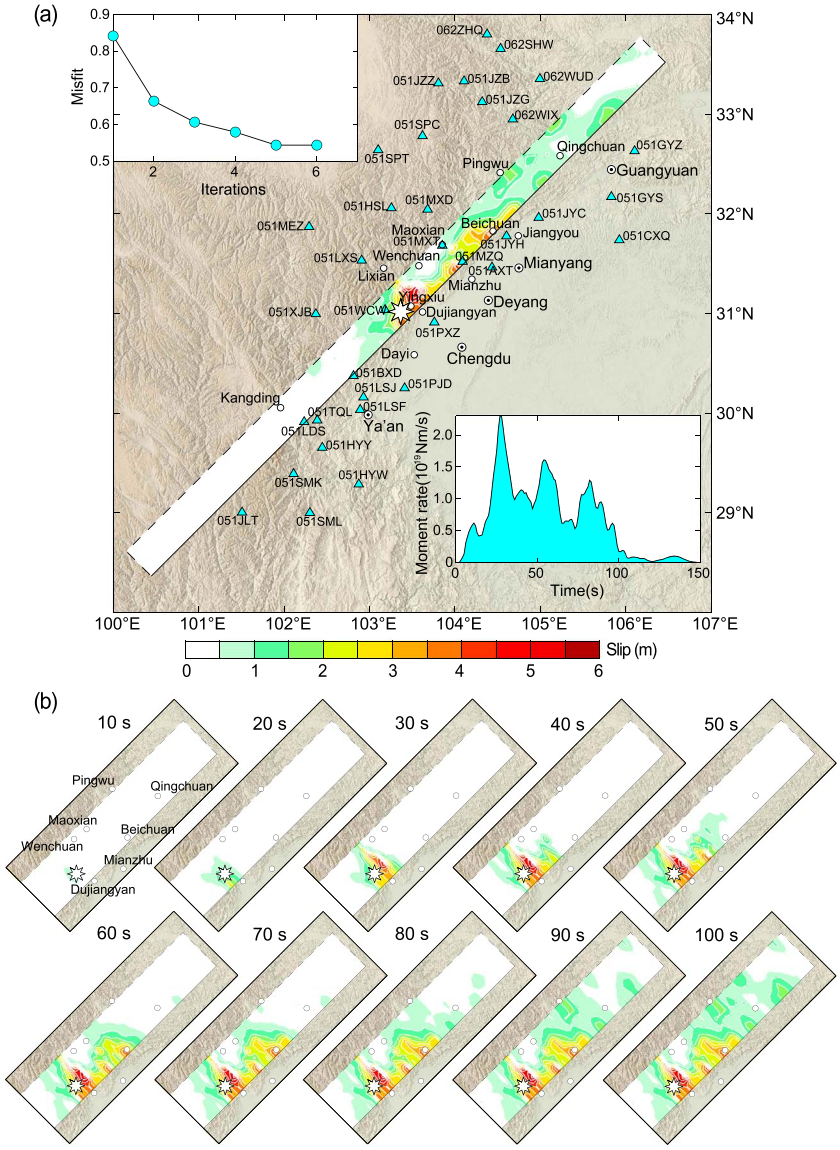

Figure 2. IDS source imaging results for the Wenchuan earthquake using the strong motion data. (a) The misfit curve of (top left) the iterations and (bottom right) the source time function, strong motion stations (cyan triangles), and the surface projection of fault slip distribution. (b) Snapshots of the temporal variations of the fault slip distribution. The stars in Figures 2a and 2b denote the epicenter.

which are most used currently, it is solved through the preestimated fault size and/or the moment minimization. Step 6 is the smoothing constraint, which is also commonly used in most geophysical inversions. Using the smoothing rule, the update slip distributions during the iterations have about the same characteristic roughness as obtained after the first iteration without smoothing. The idea behind this rule is that a single iteration of the IDS approach is comparable with backprojection, leading to a result which roughly reflects the resolution ability of the network. It is noted that the frequency bands employed in the IDS and backprojection are different. If the network coverage around the fault is adequate and the rupture is simple enough, a single iteration might be sufficient to obtain the major characteristics of slip distribution.

Additionally it should be noted that in the above algorithm, the time/frequency domain is not expressed in a discrete form. In fact, the IDS method can work with arbitrarily small time intervals without any negative effect on the solution stability. This feature is different to the conventional linear algorithm. On the other

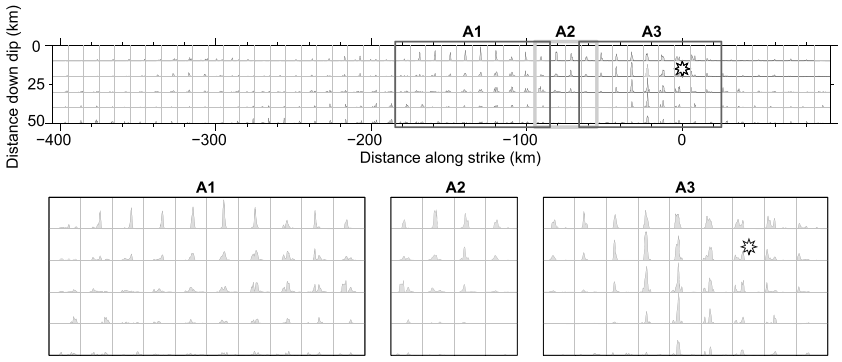

Figure 3. (top) Subfault STFs (slip rate) obtained from the IDS inversion of the strong motion data for the Wenchuan earthquake. In each patch, the *x* axis is the time, and the *y* axis is the STF value. The time window showing the STFs is 100 s, and the maximum slip rate is 0.6 m/s. (bottom) The three zoomed slip asperities.

hand, it differs from the conventional nonlinear algorithm; in that, the form of the ESTFs is not preselected, but derived directly from the data.

A priori source information used in the IDS method includes the hypocenter location, the focal mechanism, and the fault geometry. In addition, we assume that the rupture propagation can never exceed the *P* wave velocity and that each subfault can rupture until the time when there is no significant waveform energy left in the observations. In this study, if not otherwise specified, the Green's functions are calculated using the code "Qseis" of *Wang* [1999] and are based on the seismic reference model AK135 [*Kennett et al.*, 1995], modified with the local crustal structure adopted from CRUST2.0 [*Bassin et al.*, 2000].

In the following, we apply the new method to the 2008 Wenchuan and 2011 Tohoku earthquakes, since their ground motion was well recorded by near-field strong motion and/or high-rate GPS networks.

3. The 2008 M_w7.9 Wenchuan Earthquake

The hypocenter of the 12 May 2008 Wenchuan earthquake, which occurred at 06:27:57.59 UTC, is located at (30.018°N, 103.365°E) at a depth of 15.5 km [*Yang et al.*, 2012]. We adopt the focal mechanism of strike = 225°, dip = 39°, and rake = 120° from *Zhang et al.* [2009] and select a large enough potential rupture area of about 810 km long and 50 km wide, consisting of 81 × 5 = 405 subfaults, each 10 km × 10 km in size (Figure 2a). The Wenchuan earthquake was well recorded by the local strong motion network distributed along the ruptured fault. We choose 36 stations with an average station distance of about 50 km (Figure 2a). The selected accelerograms are integrated to velocity seismograms and then filtered by a band-pass filter of 0.02–0.10 Hz.

Using the IDS method, the moment magnitude of the earthquake converges at M_w7.97 after only six iterations, which is consistent with the GCMT solution (about 0.05 more). Although the potential fault length is chosen to be as large as 810 km, most of the detected rupture is located along the northeast segment of the fault, confirming that the earthquake fault ruptured unilaterally. The fault slip extends about 300 km, and the slip maxima appear mostly in the shallowest patches, indicating that the fault slip may have broken the surface. The peak slip value is about 5.8 m, 30 km northeast of the epicenter, where the largest surface rupture was observed [*Xu et al.*, 2009]. Three major slip patches were found to be located near Beichuan, Mianzhu, and Yingxiu, respectively, consistent with reports that the most serious damage occurred in these regions. There is also a slip gap on the fault about 100 km northeast of the epicenter (near station 051MZQ; Figure 2a), consistent with other studies [*Zhang et al.*, 2009; *Shen et al.*, 2009; *Xu et al.*, 2010; *Wang et al.*, 2011; *G. Zhang et al.*, 2012]. In the first 20 s, the slip initiated around the hypocenter and did not show any dominant rupture directions (Figure 2b). From 30 s, the ruptures began to propagate to the NE unilaterally at a shallow depth, reaching Mianzhu and Beichuan at 40–50 s and 50–60 s, respectively. After 70 s, the rupture became relatively weak and scattered, but still propagated to the NE. However, our results show that the rupture did not continuously propagate to the northeast. As shown in Figure 3, some subfault STFs around the hypocenter demonstrate two peaks, indicating that the rupture first propagated from the hypocenter to the northeast and then began to rupture to the southwest. The repeated northeast-southwest rupture around the hypocenter is significant and resulted in

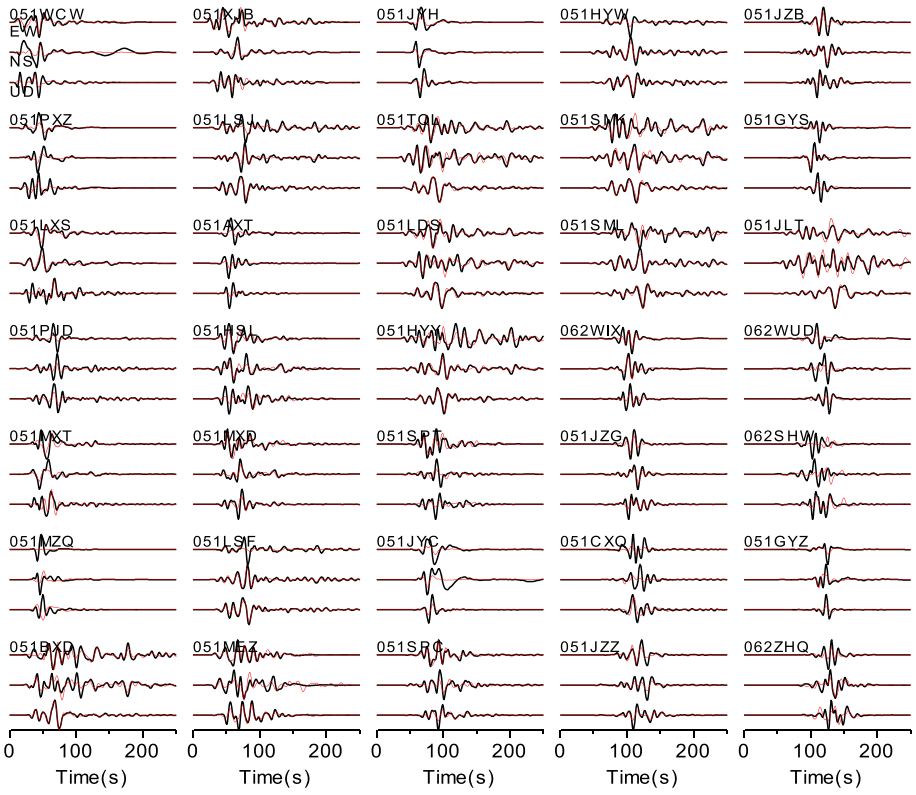

Figure 4. Comparisons of the observed (black) and synthetic (red) seismograms of the strong motion data for the Wenchuan earthquake.

the largest subevent occurring around 25 s after the rupture initiation, which is consistent with previous studies [*Zhang et al.*, 2009]. Because there are at least two parallel faults near the epicenter that ruptured during the earthquake [*Xu et al.*, 2009], the northeast and southwest rupture propagations in the first 40 s may not have occurred on the same fault [*Hartzell et al.*, 2013]. The peak slip rate reached about 0.6 m/s and occurred at locations about 30 km and 130 km to the northeast of the hypocenter. The maximum slip is (5.8 m) less than the value of 8–10 m determined from the near-field geodetic data [*Shen et al.*, 2009; *Xu et al.*, 2010] but is more consistent with the observed surface ruptures [*Xu et al.*, 2009]. The source time function obtained in this study (lower right inset, Figure 2a) shows that the rupture process lasted about 100 s.

The misfit (σ^2) is 0.54 (i.e., acceptable according to our criteria above; Figure 4). Large discrepancies appear for a few stations, such as 051WCW and 051JYC, whose baseline shifts on the NS component could not be sufficiently removed by the band-pass filter, and 051MZQ, which is very close to the fault trace such that any uncertainties in the fault location and geometry can cause large errors in the synthetic seismograms.

Although only strong motion data were used for the 2008 Wenchuan earthquake, both the slip distribution and the source time function are consistent with the results obtained by the joint inversion of the GPS and interferometric synthetic aperture radar data [*Shen et al.*, 2009; *Wang et al.*, 2011] or all available seismic and geodetic data [*Hartzell et al.*, 2013]. However, there is a significant difference in the peak slip, which is about 5.8 m in our results, less than most of the previous studies but is closer to the results from the field investigations [*Xu et al.*, 2009]. It should be pointed out that we have chosen a long enough potential fault; i.e., no constraint on the fault size was assigned. This would be helpful for the rapid response of earthquake emergency and EEW, in which a very little information about the rupture length and direction is available in the earliest stages. Additionally, it should be noted that for the purpose of rapid response, the rupture process is usually estimated on a single-fault plane. In the case of the Wenchuan earthquake, many previous studies indicated that its rupture process involved multiple complex faults. This feature is reflected by some apparent multiple or repeated ruptures in our single-fault results.

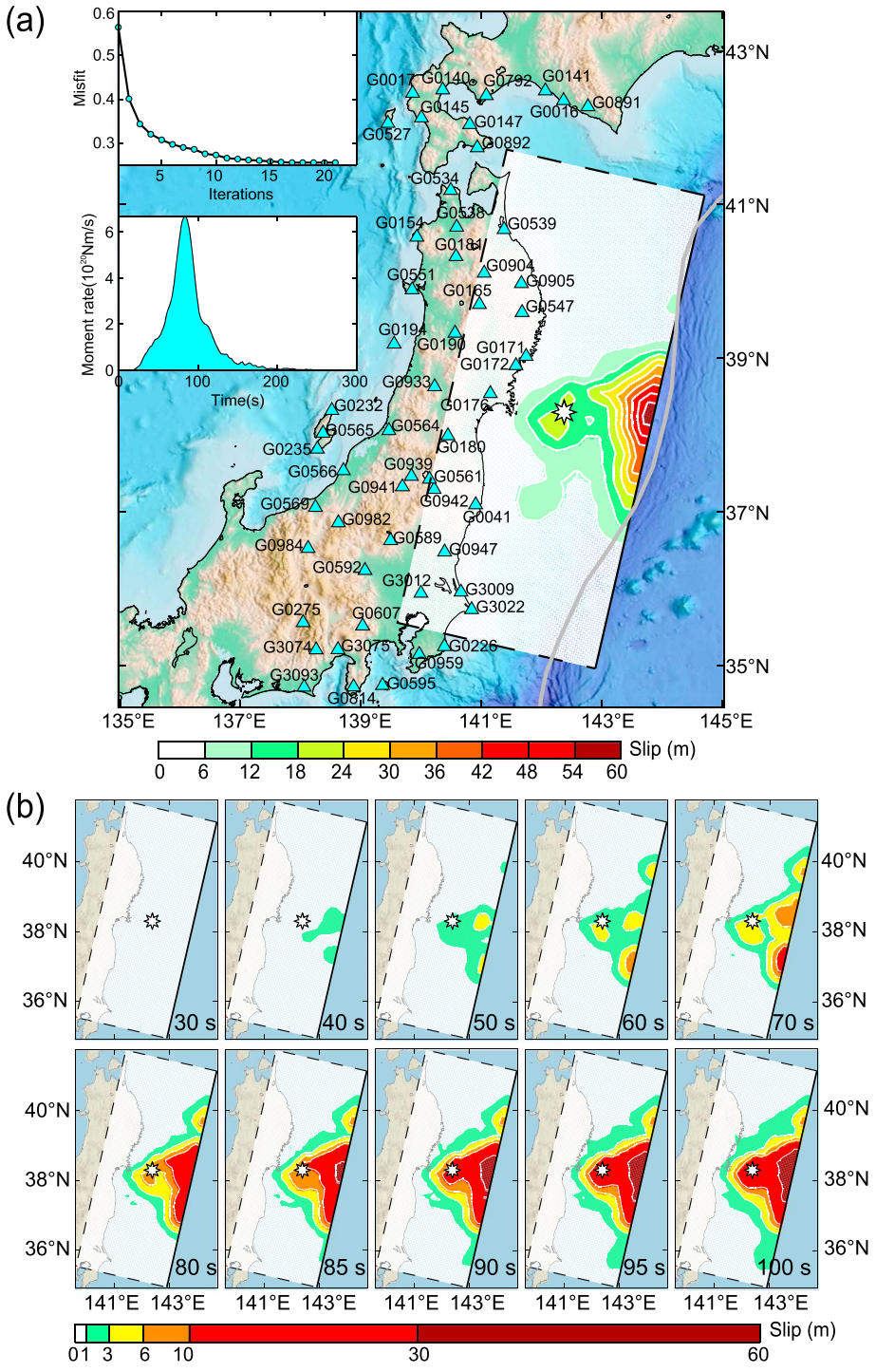

Figure 5. IDS source imaging results for the Tohoku earthquake using the high-rate GPS data. (a) The misfit curve of (upper left) the iterations and (lower right) the source time function, GPS stations (cyan triangles), and the surface projection of fault slip distribution. (b) Snapshots of the temporal variations of the fault slip distribution projected to the surface. The stars in Figures 5a and 5b denote the epicenter.

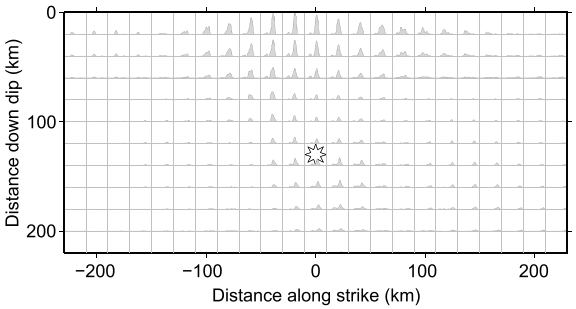

Figure 6. Subfault STFs (slip rate) of the Tohoku earthquake. In each patch, the *x* axis is the time, and the *y* axis is the STF value. The time window showing the STFs is 150 s, and the maximum slip rate is 2.4 m/s. The star denotes the hypocenter.

4. The 2011 M_w9.0 Tohoku Earthquake

The Tohoku earthquake nucleated at (38.297°N, 142.372°E) at a depth of 30 km on 11 March 2011 at 05:46:24 UTC, with a fault plane of strike = 193°, dip = 14°, and rake = 81° (W phase solution of USGS). The latter is consistent with the tectonics of the Japan Trench as a well-known tsunamigenic subduction thrust fault. We select a large potential rupture area on this fault with a length of 700 km and width of 300 km, consisting of $35 \times 15 = 525$ subfaults, each 20 km × 20 km in size (Figure 5a).

We choose 55 high-rate GPS stations, each of which contains three-component displacement seismograms, randomly from 414 stations with an average interstation distance of about 70 km (Figure 5a). The displacement records are differentiated to velocity seismograms and then filtered by a low-pass filter of 0–0.05 Hz.

Figure 5 shows the inversion results for the Tohoku earthquake. After 21 iterations (inset in Figure 5a), the seismic moment converges at about 4.65×10^{22} Nm, equivalent to a moment magnitude of M_w9.05. The total rupture process lasted as long as 200 s, with 80% of the energy released between 50 and 120 s (inset in Figure 5a). The major rupture area (Figure 5a) is located at a very shallow depth, consistent with other studies [*Lee et al.*, 2011; *Shao et al.*, 2011; *Y. Zhang et al.*, 2012a]. The maximum slip determined is close to 60 m, which is larger than some results derived from jointly inverting teleseismic waveform and inland coseismic GPS data [*Y. Zhang et al.*, 2012a], but close to the result of *Wang et al.* [2013] based on the inversion of inland and seafloor coseismic GPS data and that of *Lee et al.* [2011], who jointly inverted teleseismic, strong motion, and high-rate GPS waveform data.

Many subfault STFs of the Tohoku earthquake show multirupture features (Figure 6), supporting the findings of *Lee et al.* [2011]. The whole rupture process can be roughly characterized by two events (Figure 5b). The first one initiated around the hypocenter, propagated along the updip direction, and broke the seafloor. The cumulative slip of this event is estimated to be less than 6 m. The second is the major event of the earthquake, which occurred at a shallow depth and lead to the maximum slip (~57 m) near the trench. Because of the coverage of the GPS network on only one side of the rupture, earlier signals near the trench are not easily distinguished from later rupture signals in the deeper area toward the coast. This may explain why the peak moment rate at 85 s appears later here than is resolved from teleseismic inversions [*Y. Zhang et al.*, 2012a; *Lee et al.*, 2011].

The misfit of the inversion is about 0.26 (i.e., good, according to our criteria discussed above). From Figure 7, the data fits with the high-rate GPS seismograms are fairly good, except for the three northeastmost GPS stations (G0141, G0016, and G0891; Figure 5b), whose records show very long coda waves, probably caused by local basin effects (Figure 7).

The Tohoku earthquake was also well recorded by the strong motion network KiK-net. For the rupture process inversion, the only difference in the data processing between the high-rate GPS and the strong motion data is that the latter needs to be additionally high-pass filtered to remove the bias caused by their baseline errors [*Wang et al.*, 2013]. We also applied the IDS method to the strong-motion-based velocity seismograms in the frequency band of 0.02–0.05 Hz and obtain results similar to those from the high-rate GPS network (see Figures 12–14 in the supporting information), noting that the earth structure used for the high-rate GPS and strong motion data inversions are the same. The obtained scalar moment is about 4.30×10^{22} Nm, equivalent to a moment magnitude of M_w9.03. The peak slip is estimated to be 51 m. Probably because of the lack of very low frequency content (<0.02 Hz) in the strong motion data, both the peak slip and the moment magnitude are slightly smaller than those from the high-rate GPS data.

An interesting question for the Tohoku earthquake is whether the slip reaches the trench. This source characteristic could not be estimated well using the static coseismic displacement data from the GPS measurements, since all of the GPS Earth Observation Network stations are located on the westside of the trench. In comparison, the waveform inversion has a better resolution because of the Doppler effects

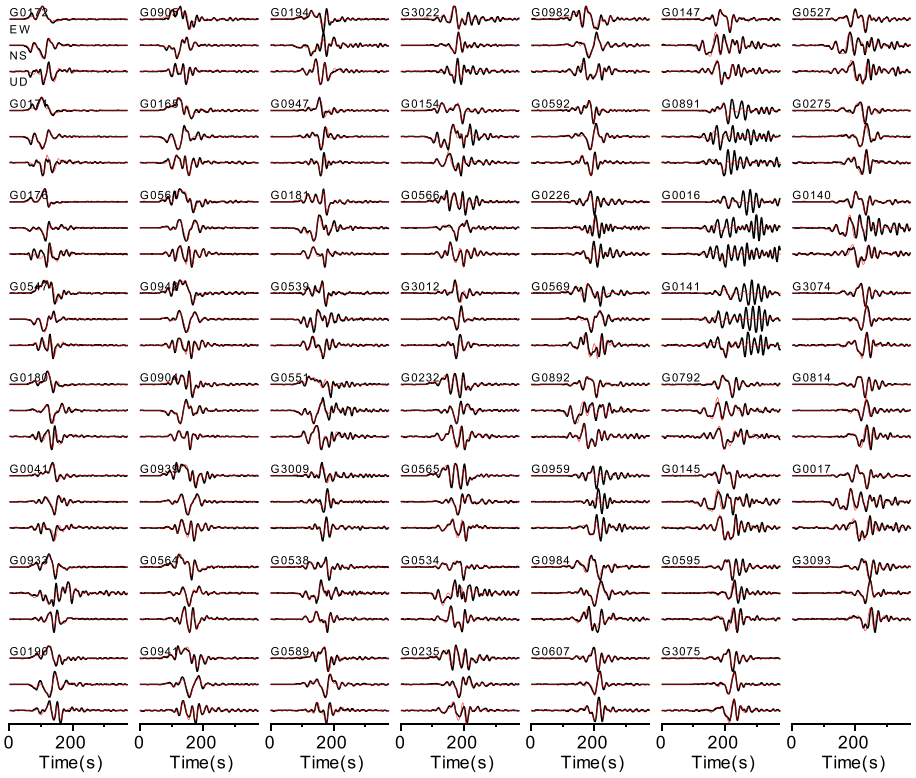

Figure 7. Comparisons of the observed (black) and synthetic (red) high-rate GPS seismograms from the Tohoku earthquake.

contained in the high-rate GPS and strong motion seismograms. Based on our results, the slip maxima occurred at a very shallow depth and reached at least 50 m. This indicates that the ruptures might have broken the seabed, consistent with the observation of results of repeated multibeam bathymetric surveys [*Fujiwara et al.*, 2011].

5. Resolution Tests for the 2008 Wenchuan and 2011 Tohoku Earthquakes

We conducted resolution tests on the strong motion network for the Wenchuan earthquake and the high-rate GPS network for the Tohoku earthquake, respectively. In these tests, synthetic data are generated based on the assumed rupture models, to which we added 10% Gaussian noise. A constant rupture velocity (3 km/s for the Wenchuan earthquake and 2 km/s for the Tohoku earthquake) is used in all the input models. When inverting the synthetic data with the IDS method, the maximum rupture velocity is allowed to be as large as the *P* wave velocity and the rupture duration as long as necessary, implying that practically no assumption on the rupture process is needed.

In the first resolution test (Figure 8) on the strong motion network for the Wenchuan earthquake, four rectangular slip asperities, each with a single triangular subfault STF, are defined on the fault (Figures 8a and 8c). The input and estimated slip and subfault STFs are compared in Figures 8a–8d. The comparison shows that the moment magnitude, fault slip, and the shapes of the subfault STFs are all well retrieved using the IDS method, indicating the reliability of the rupture process that we have reconstructed for this event.

For the other resolution test performed on the high-rate GPS network of the Tohoku earthquake (Figure 9), the earthquake is represented by two rectangular slip asperities at different depths (Figure 9a). To simulate the multiruptures, the subfault STF, in contrast to the Wenchuan earthquake test, is represented by twin triangles (Figure 9c). Additionally, we recognize that the hypocenter location can be biased by up to several tens of kilometers for subduction events because of the one-sided network coverage. Therefore, the "true" hypocenter location in this test is offset 45 km (grey star in Figures 9b and 9d), corresponding to a conservative estimate of the rapid location error for such subduction zone earthquakes. Comparing the input and estimated rupture

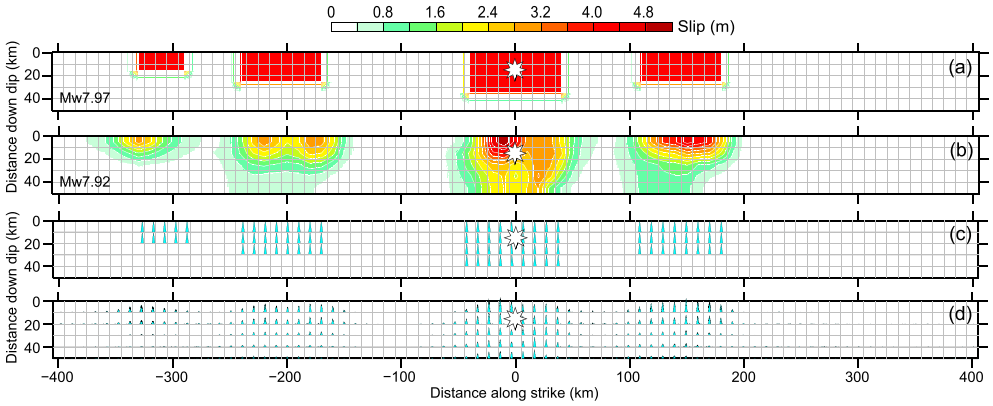

Figure 8. Resolution test for the Wenchuan earthquake. (a) The input slip distribution. (b) The resolved slip distribution by the IDS method. (c) The input STFs of all the ruptured subfaults. (d) The resolved STFs. The stars denote the hypocenter. In each patch in Figures 8c and 8d, the *x* axis is the time, and the y axis is the STF value. The time window showing STFs is 160 s.

models shows that even with the strongly biased hypocenter estimate, the two slip asperities and their twin triangular STFs are well resolved.

6. Comparison With the Conventional Inversion Method

We compare the IDS method with the conventional linear network inversion (LNI) method for the rupture imaging of the Wenchuan and Tohoku earthquakes. To stabilize the solution, the LNI method generally needs to specify the weights of different physical constraints. In the code of *Y. Zhang et al.* [2012b] used for the following tests, three physical constraints, which contain the spatial smoothing, temporal smoothing, and moment minimization, have to be specified with three weighting factors. After certain scaling, the two smoothing factors usually vary between 0 and 50, and the moment-minimizing factor takes a value between 0 and 1. Generally these weighting factors depend on the resolution capability of the network used. A poorly distributed network requires relatively stronger physical constraints to ensure the reasonability and stability of the inversion results. In practice, however, the weighting factors can only be optimized empirically using the trial-and-error approach so that a certain subjective influence on the results is often not avoidable.

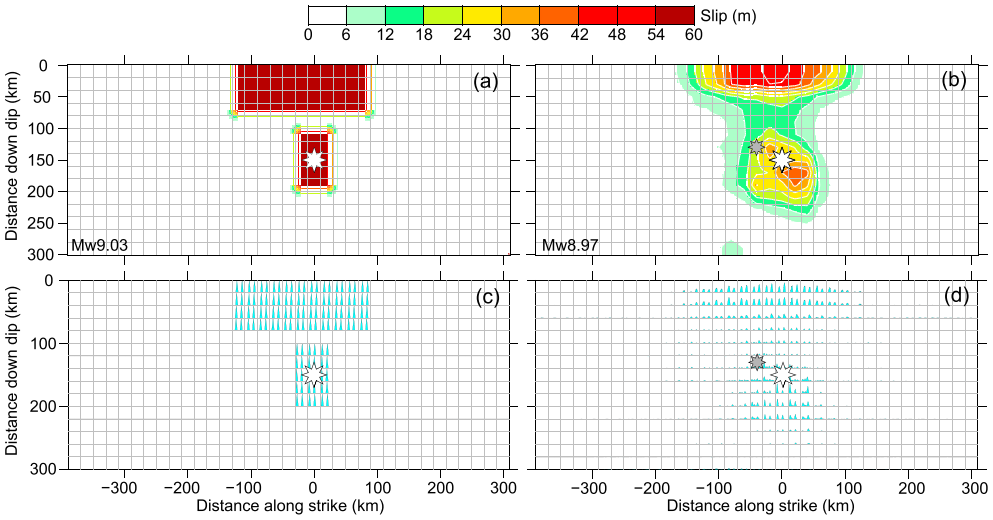

Figure 9. Resolution test for the Tohoku earthquake with a large bias in the hypocenter location (grey star, 45 km away from the true location). (a) The input slip distribution. (b) The resolved slip distribution by the IDS method. (c) The input STFs of all the ruptured subfaults. (d) The resolved STFs. The stars denote the hypocenter. In each patch in Figures 9c and 9d, the *x* axis is the time, and the *y* axis is the STF value. The time window showing STFs is 200 s.

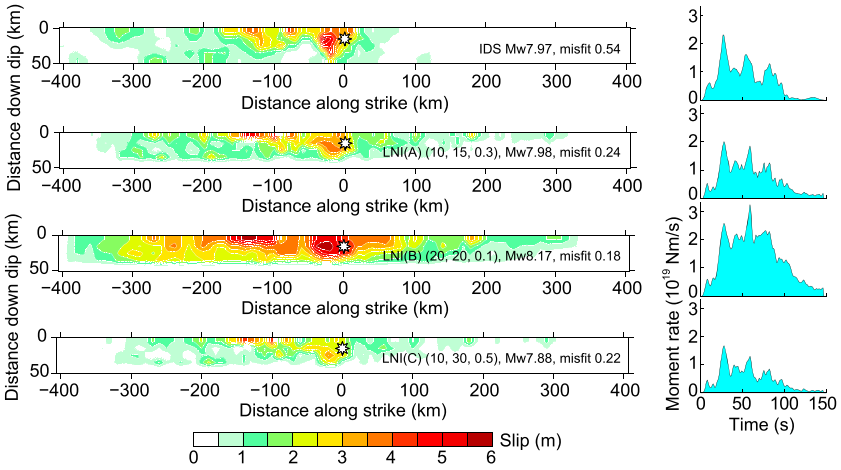

Figure 10. Comparisons of (left) the slip models and (right) the source time functions obtained with the IDS and LNI methods applied to the strong motion data for the Wenchuan earthquake. The first row shows the results of the IDS method, and the second row is the preferred results of the LNI method with proper constraint weights. The third and fourth rows show the other two results of the LNI method obtained during the trials carried out to optimize the constraint weights. The three weighting factors for spatial and temporal smoothing and moment minimizing are given in the parentheses. The stars denote the hypocenter.

We use the same parameterizations for the LNI method as used for the IDS method. The maximum rupture velocity is set uniformly to 6 km/s (the *P* wave velocity in the upper crust), and the rupture duration is not limited for each subfault. In the case of the Tohoku earthquake, we downsampled the high-rate GPS data from 1 to 0.25 samples per second in order to reduce the required computational effort for the LNI method. Since the cutoff frequency is 0.05 Hz, this downsampling would not miss any effective waveform information.

For each of the two earthquakes, the LNI method is tested for three different combinations of the three constraining weighting factors (denoted as LNI (A), LNI (B), and LNI (C)), and the results obtained are compared with those of the IDS method (Figures 10 and 11). For the Wenchuan earthquake, the combination of 20, 20, and 0.1 for the three constraining weighting factors leads to a smoothed fault slip distribution and overestimated moment magnitude, while the combination of 10, 30, and 0.5 results in an underestimated moment magnitude compared to the model of IDS model. After several trials by empirically adjusting the three weights, we arrive at the combination of 10, 15, and 0.3, which best estimates the fault slip distribution and moment magnitude (Figure 10) and appears to be the most reasonable based on recent studies [*Shen et al.*, 2009; *Wang et al.*, 2011] and the IDS results. For the Tohoku earthquake, the finally preferred weighting factor combination is 0.1, 15, and 0.0, yielding a rupture area of 300–400 km along the strike and 150–200 km along the dip, with the largest asperity at a shallow depth close to the trench and a moment magnitude of M_w9.0, all of which are consistent with the results of other independent studies (Figure 11).

Since the LNI method is based on least squares optimization, its data fits are generally better than those of the IDS method. In the case of the Tohoku earthquake, for example, the relative misfit we obtained with the IDS method is 0.26. When using the LNI method, the relative misfit is slightly improved to 0.10–0.19, depending on the choice of empirical parameters for the physical constraints. In the case of the Wenchuan earthquake, the data fit achieved by the LNI method is about 0.3 less compared with that derived by the IDS method. The reason is the narrow and relatively higher frequency range (0.02–0.10 Hz) of the strong motion data, which can be better explained by the least squares optimization, although not necessarily also more reasonably than the direct imaging. In fact, the slip models obtained by the LNI method depend strongly on the choice of the three physical constraints, and most of them appear less consistent with the results of recent studies if the three weighting factors were not properly specified. The trade-off problem related to the physical constraints is well known for conventional inversions with either linear or nonlinear algorithms. So far, the weighting of the physical constraints is often optimized manually, leading to difficulties when attempting the automatic use of this method. We note that there have been several studies suggesting the so-called BIC (Bayesian information criterion) optimization of the physical constraints [e.g., *Akaike*, 1980; *Yagi et al.*, 2004; *Fukuda and Johnson*, 2008], which can, in principle, be automatized. In the present case,

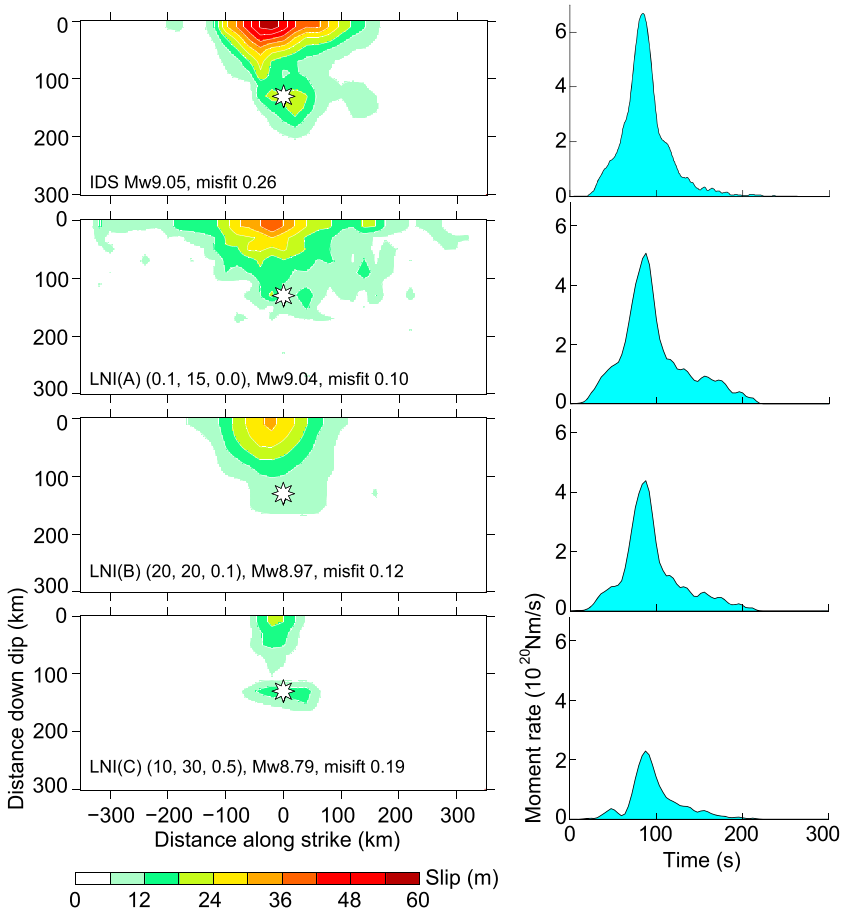

Figure 11. Same as Figure 10 but using the high-rate GPS data for the Tohoku earthquake.

however, the BIC approach would mean a grid search process for a multiparameter space that would generally require a considerably larger computational effort.

7. Discussion and Conclusions

One particular advantage of the IDS method over traditional methods is that it can easily retrieve complex rupture processes in a straightforward way, which cannot be easily done when using the nonlinear inversion method. Normally, the linear inversion method can be adopted to resolve multiple ruptures, although such capability is generally limited because it can affect the numerical stability. Using the IDS method, no empirical constraint needs to be changed dependent on different earthquakes. The two case studies and the resolution tests presented above have demonstrated the robustness of this new approach for the inversion of complete near-field seismograms.

In addition, the IDS method is considerably more efficient than the LNI method. The IDS and LNI codes we used for the comparison are written in MATLAB. Neither is specially parallelized but can make use of all CPU cores by using the distributed computing toolbox of MATLAB. Without any optimization of the empirical constraints, the CPU time required by the LNI method on an Intel i7-3770 PC is 1140 s for the Wenchuan earthquake and 1060 s for the Tohoku earthquake, in comparison to 5 s and 35 s for the IDS method, respectively. It should be noted that the deconvolution and stacking procedures are computed independently from subfault to subfault. Since such calculations are easily parallelized, the computational effort required by the IDS algorithm should not be a problem when integrated into an EEW system.

In general, we can make a theoretical comparison of the computational efforts required by the IDS and linear network inversion (LNI) methods. There are three factors impacting upon the computation time, namely, the

number of waveform data channels N_w, the number of subfaults N_s, and the number of time samples N_l of both waveform data and subfault STFs. For the IDS method, the computation effort is estimated to be $O(N_w \cdot N_s \cdot N_l \log N_l)$, where the factor $N_l \log N_l$ is known to be related to the fast Fourier transform needed for the convolution and deconvolution. For the LNI method, since the inversion of a $M \times N$ matrix needs the time $O[\min(M^2 \cdot N, M \cdot N^2)]$, the total computation effort becomes $O\left[N_l^3 \cdot \min\left(N_s^2 \cdot N_w, N_s \cdot N_w^2\right)\right]$. Note that to achieve as high temporal resolution as possible, the subfault STFs should have the same sampling rate as the waveform data. Thus the number of time samples impacts upon the number of both rows and columns of the inversion matrix, leading to the factor N_l^3. Additionally, in contrast to the LNI method, the major computation part (i.e., convolution and deconvolution) of the IDS method is independent for different stations and subfaults, implying that it can be easily parallelized. If the nonlinear network inversion method is used, the computation effort is even considerably larger than the LNI inversion method.

An issue of the IDS method to be considered is the physical constraint on the roughness of the inferred slip distribution. We solved this problem by an empirical rule (see step 6 of the pseudo algorithm), which has been tested in many synthetic tests and the present two case studies. For both the Wenchuan and Tohoku earthquakes, it yields peak slip values that are acceptable when considering other independent studies. Without this smoothing step, the peak slip would be overestimated by a factor of 2–3. The peak slip value can also be affected by the choice of the sensitivity factor (see step 5 of the pseudo algorithm). However, other relevant source characteristics, such as magnitude, fault size, location of the major slip asperity, rupture propagation, and duration, which are all useful for early warning and hazard assessments, are not significantly dependent on the empirical constraints used here.

The water level is the only parameter that could be changed but is fixed in the IDS method. For numerical stability, we suggest a relatively large water level parameter for deconvolving the data with synthetic Green's functions, because this leads to only the most significant rupture signals being retrieved during the iterations. If the water level is too small, overestimated slip may occasionally appear in earlier iterations, which cannot be corrected in the subsequent iterations because of the imposed positivity constraint (see step 3 of the pseudo algorithm). By using a large water level parameter, this effect can be sufficiently minimized. In the present two case studies (and many other tests not shown here), we found that no substantial change in the inversion results if the water level parameter ε used in equation (6) is larger than 0.05 (see Figures 15 and 16 in the supporting information). Therefore, we can fix the water level at 0.1 to ensure the automaticity of IDS method.

We have also tested the IDS method for teleseismic inversions. In this case, when using conventional inversion methods, a general problem is that the synthetic Green's functions based on a standard Earth model have large uncertainties in travel times. Consequently, it is difficult to accurately resolve the rupture distribution absolutely. The same problem also exists when using the IDS method. Hence, similarly to conventional inversion methods, we shift the *P* wave arrival time of the data so that it is consistent with the Earth model used and attempt to resolve the rupture distribution relative to the given hypocenter. For the Wenchuan and Tohoku earthquakes, the teleseismic rupture models produced by the IDS method are consistent with those from the near-field data inversions, except for slightly underestimated magnitudes, lower spatial resolutions, and underestimates of the peak slips (see Figures 17–22 in the supporting information). These underestimations may be associated with the low resolution of the teleseismic networks compared to the near-field networks. For very large earthquakes such as the Tohoku event, because of the lack of low and zero frequencies, the moment magnitude as well as the peak slip were underestimated using teleseismic waveform data. We note that in order to test the robustness of the new method for teleseismic inversions, all of the parameters for the physical (empirical) constraints are fully adopted from those used for the near-field data inversions. The same is also true for the cutoff frequencies applied to the data (0.01–0.1 Hz for the Wenchuan earthquake and 0.01–0.05 Hz for the Tohoku earthquake) and the model parameterizations. In particular, we note the significant differences between the teleseismic results of the IDS method and the backprojection method. The latter generally only recovers the high-frequency source signals along the deep edge of the ruptured area [*Honda et al.*, 2011; *Meng et al.*, 2011; *Yao et al.*, 2011]. Such information is interesting for understanding the earthquake nucleation process but less relevant for tsunami early warning.

We recognize that there are still a few practical issues and limitations for the application of the IDS method to EEW. First, while existing EEW systems can determine the hypocenter in real time, they are generally not able

Table 1. Subfault Sizes and Cutoff Frequencies Suggested for the Real-Time Source Imaging

M_w	Subfault Size (km)	Cutoff Frequency (Hz)
6.5–7.5	5	0.2
7.5–8.5	10	0.1
8.5–9.5	20	0.05

to provide an equally rapid focal mechanism. Fortunately, many large earthquakes occur on existing faults with well-known mechanisms. For example, the focal mechanisms of the Wenchuan earthquake and the Tohoku earthquake are both consistent with the tectonic background of their epicentral regions. Especially, for most tsunamigenic subduction earthquakes, the fault geometries have been well determined [*Hayes et al.*, 2012]. There are also some special earthquakes with an unexpected mechanism controlled by the regional tectonics that were not very clear previously, such as the 2013 M_w8.6 Sumatra earthquake [*Yue et al.*, 2012]. Therefore, for EEW in a given area, the mechanisms of the seismogenic faults should be carefully investigated (e.g., by geological investigations into inland earthquakes). Once an earthquake over a certain threshold magnitude (for example, M_w6.5) is detected and well located, we can therefore immediately determine which fault has ruptured and thus assume a corresponding mechanism. For this case, uncertainties of the hypocenter location may impact upon the selections of the ruptured fault and its mechanism. Thus, a densely distributed network would be required to reduce the location uncertainties. In addition, it would be useful to extend the IDS method with a module for rapid mechanism estimation using, e.g., the approach suggested by *Melgar et al.* [2013]. Second, it should be noted that the fault size, subfault size, and the cutoff frequency used in the present case studies are fixed. In EEW, however, since we do not have the knowledge of the final magnitude of the earthquake, these three parameters need to be adjusted during the real-time inversions. In most cases, a large enough potential fault size can be fixed based on the tectonic setting of interest. To achieve an appropriate resolution, the subfault size and frequency band can be changed dynamically, depending on the increased earthquake magnitude detected during the real-time analysis. For example, supposing that the lowest moment magnitude of disastrous earthquakes is about M_w6.5, we can first use the subfault size of 5 km and cutoff frequency of 0.2 Hz ($f_{\mathrm{cut}} \sim \frac{1}{4}\frac{V_s}{\Delta L}$, where V_s is the S wave velocity and ΔL is the subfault length [see, e.g., *Heimann*, 2010], respectively. Once the moment magnitude exceeds M_w7.5, for example, the subfault size can be increased to 10 km, and the cutoff frequency can be decreased correspondingly to 0.1 Hz, and the inversion performed once more. If the moment magnitude further exceeds M_w8.5, the subfault size and cutoff frequency can be updated again until the moment magnitude converges (Table 1).

In summary, the IDS method presented in this paper shows its robustness both in synthetic tests and in its application to the case studies of the 2008 Wenchuan and 2011 Tohoku earthquakes. In particular, this approach does not need any manual adjustment of the physical (empirical) constraints and has the ability to automatically image earthquake sources using either near-field or teleseismic waveform data. This may have an important impact on the development of future earthquake and tsunami early warning and rapid response systems.

Acknowledgments

This paper is funded by the REAKT project (Towards Real-Time Earthquake Risk Reduction) of the European Seventh Framework Programme (grant agreement 282862). The strong motion and GPS data for the Tohoku earthquake were provided by the National Research Institute for Earth Science and Disaster Prevention and the Geospatial Information Authority of Japan, respectively. The strong motion data for the Wenchuan earthquake were provided by the China Strong Motion Networks Center. We thank Martin Mai, Gavin Hayes, and another anonymous reviewer for their constructive comments. Kevin Fleming proofread the manuscript.

References

Akaike, H. (1980), Likelihood and Bayes procedure, in *Bayesian Statistics*, edited by J. M. Bernardo et al., pp. 143–166, Univ. Press, Valencia, Spain.

Allen, M. R., P. Gasparini, O. Kamigaichi, and M. Bose (2009), The status of earthquake early warning around the world: An introductory overview, *Seismol. Res. Lett.*, *80*(5), 682–693, doi:10.1785/gssrl.80.5.682.

Allmann, B. P., and P. M. Shearer (2007), A high-frequency secondary event during the 2004 Parkfield earthquake, *Science*, *318*, 1279–1283, doi:10.1126/science.1146537.

Bassin, C., G. Laske, and G. Masters (2000), The current limits of resolution for surface wave tomography in North America, *Eos Trans. AGU*, *81*, F897.

Chen, Y., and L. Xu (2000), A time-domain inversion technique for the tempo-spatial distribution of slip on a finite fault plane with applications to recent large earthquakes in the Tibetan Plateau, *Geophys. J. Int.*, *143*, 407–416.

Dreger, D. S. (1994), Empirical Green's function study of the January 17, 1994 Northridge, California earthquake, *Geophys. Res. Lett.*, *21*, 2633–2636, doi:10.1029/94GL02661.

Ekström, G., M. Nettles, and A. M. Dziewoński (2012), The global CMT project 2004-2010: Centroid-moment tensors for 13,017 earthquakes, *Phys. Earth Planet. Inter.*, *200-201*, 1–9, doi:10.1016/j.pepi.2012.04.002.

Fujiwara, T., S. Kodaira, T. No, Y. Kaiho, N. Takahashi, and Y. Kaneda (2011), The 2011 Tohoku-Oki earthquake: Displacement reaching the trench axis, *Science*, *334*, 1240, doi:10.1126/science.1211554.

Fukuda, J., and K. M. Johnson (2008), A fully Bayesian inversion for spatial distribution of fault slip with objective smoothing, *Bull. Seismol. Soc. Am.*, *98*, 1128–1146.

Graves, R. W., and A. Pitarka (2010), Broadband ground-motion simulation using a hybrid approach, *Bull. Seismol. Soc. Am.*, *100*, 2095–2123.

Guatteri, M., P. M. Mai, G. C. Beroza, and J. Boatwright (2003), Strong ground-motion prediction from stochastic-dynamic source models, *Bull. Seismol. Soc. Am.*, *93*(1), 301–313.

Hartzell, S. H., and T. H. Heaton (1983), Inversion of strong ground motion and teleseismic waveform data for the fault rupture history of the 1979 Imperial Valley, California, earthquake, *Bull. Seismol. Soc. Am.*, *73*, 1553–1583.

Hartzell, S. H., and P. Liu (1996), Calculation of earthquake rupture histories using a hybrid global search algorithm: Application to the 1992 Landers, California, earthquake, *Phys. Earth Planet. Inter.*, *95*, 79–99.
Hartzell, S. H., C. Mendoza, L. Ramirez-Guzman, Y. Zeng, and W. Mooney (2013), Rupture history of the 2008 Mw 7.9 Wenchuan, China, earthquake: Evaluation of separate and joint inversions of geodetic, teleseismic, and strong-motion data, *Bull. Seismol. Soc. Am.*, *103*, 353–370, doi:10.1785/0120120108.
Hayes, G. P., D. J. Wald, and R. L. Johnson (2012), Slab1.0: A three-dimensional model of global subduction zone geometries, *J. Geophys. Res.*, *117*, B01302, doi:10.1029/2011JB008524.
Heimann, S. (2010), A Robust Method to Estimate Kinematic Earthquake Source Parameters, PhD Thesis of University Hamburg, Germany. [Also see http://ediss.sub.uni-hamburg.de/volltexte/2011/5357/.]
Helmberger, D. V., and R. A. Wiggins (1971), Upper mantle structure of midwestern United States, *J. Geophys. Res.*, *76*, 3229–3245, doi:10.1029/JB076i014p03229.
Honda, R., and S. Aoi (2009), Array back-projection imaging of the 2007 Niigataken Chuetsu-oki earthquake striking the world's largest nuclear power plant, *Bull. Seismol. Soc. Am.*, *99*, 141–147, doi:10.1785/0120080062.
Honda, R., S. Aoi, H. Sekiguchi, and H. Fujiwara (2008), Imaging an asperity of the 2003 Tokachi-oki earthquake using a dense strong-motion seismograph network, *Geophys. J. Int.*, *172*, 1104–1116, doi:10.1111/j.1365-246X.2007.03702.x.
Honda, R., et al. (2011), A complex rupture image of the 2011 off the Pacific coast of Tohoku earthquake revealed by the MeSO-net, *Earth Planets Space*, *63*, 583–588.
Ishii, M., P. Shearer, H. Houston, and J. E. Vidale (2005), Extent, duration and speed of the 2004 Sumatra-Andaman earthquake imaged by the Hi-Net array, *Nature*, *435*, 933–936.
Ji, C., D. J. Wald, and D. V. Helmberger (2002), Source description of the 1999 Hector Mine, California, earthquake, Part I: Wavelet domain inversion theory and resolution analysis, *Bull. Seismol. Soc. Am.*, *92*, 1192–1207.
Kennett, B. L. N., E. R. Engdahl, and R. Buland (1995), Constraints on seismic velocities in the earth from traveltimes, *Geophys. J. Int.*, *122*, 108–124.
Kikuchi, M., and H. Kanamori (1982), Inversion of complex body waves, *Bull. Seismol. Soc. Am.*, *72*, 491–506.
Krüger, F., and M. Ohrnberger (2005), Tracking the rupture of the Mw = 9.3 Sumatra earthquake over 1,150 km at teleseismic distance, *Nature*, *435*, 937–939.
Lee, S. J., B. S. Huang, M. Ando, H. C. Chiu, and J. H. Wang (2011), Evidence of large scale repeating slip during the 2011 Tohoku-Oki earthquake, *Geophys. Res. Lett.*, *38*, L19306, doi:10.1029/2011GL049580.
Liu, P., R. Archuleta, and S. H. Hartzell (2006), Prediction of broadband ground-motion time histories: Frequency method with correlated random source parameters, *Bull. Seismol. Soc. Am.*, *96*, 2118–2130.
Melgar, D., W. Crowell, Y. Bock, and J. S. Haase (2013), Rapid modeling of the 2011 Mw 9.0 Tohoku-oki earthquake with seismogeodesy, *Geophys. Res. Lett.*, *40*, 2963–2968, doi:10.1002/grl.50590.
Meng, L., A. Inbal, and J.-P. Ampuero (2011), A window into the complexity of the dynamic rupture of the 2011 Mw 9 Tohoku-Oki earthquake, *Geophys. Res. Lett.*, *38*, L00G07, doi:10.1029/2011GL048118.
Mori, J., and S. H. Hartzell (1990), Source inversion of the 1988 Upland, California, earthquake: Determination of a fault plane for a small event, *Bull. Seismol. Soc. Am.*, *80*, 507–517.
Olson, A. H., and R. J. Apsel (1982), Finite faults and inverse theory with applications to the 1979 Imperial Valley earthquake, *Bull. Seismol. Soc. Am.*, *72*, 1969–2001.
Pitarka, A., P. Somerville, Y. Fukushima, T. Uetake, and K. Irikura (2000), Simulation of near-fault strong-ground motion using hybrid Green's functions, *Bull. Seismol. Soc. Am.*, *90*(3), 566–586.
Sekiguchi, H., and T. Iwata (2002), Rupture process of the 1999 Kocaeli, Turkey, earthquake estimated from strong-motion waveforms, *Bull. Seismol. Soc. Am.*, *92*, 300–311.
Shao, G., X. Li, C. Ji, and T. Maeda (2011), Focal mechanism and slip history of the 2011 Mw 9.1 off the Pacific coast of Tohoku earthquake, constrained with teleseismic body and surface waves, *Earth Planets Space*, *63*, 559–564.
Shen, Z. K., J. Sun, P. Zhang, Y. Wan, M. Wang, R. Bürgmann, Y. Zeng, W. Gan, H. Liao, and Q. Wang (2009), Slip maxima at fault junctions and rupturing of barriers during the 2008 Wenchuan earthquake, *Nat. Geosci.*, *2*, 718–724.
Tinti, E., E. Fukuyama, A. Piatanesi, and M. Cocco (2005), A kinematic source-time function compatible with earthquake dynamics, *Bull. Seismol. Soc. Am.*, *95*(4), 1211–1223.
Vallée, M. (2004), Stabilizing the empirical Green's function analysis: Development of the projected Landweber method, *Bull. Seismol. Soc. Am.*, *94*, 394–409.
Velasco, A., C. Ammon, and T. Lay (1994), Empirical Green's function deconvolution of broadband surface waves: Rupture directivity of the 1992 Landers, California (Mw7.3) earthquake, *Bull. Seismol. Soc. Am.*, *84*, 735–750.
Wang, Q., X. J. Qiao, Q. G. Lan, F. Jeffrey, S. Yang, C. Xu, Y. L. Yang, X. Z. You, K. Tan, and G. Chen (2011), Rupture of deep faults in the 2008 Wenchuan earthquake and uplift of the Longmen Shan, *Nat. Geosci.*, *4*, 634–640, doi:10.1038/ngeo1210.
Wang, R. (1999), A simple orthonormalization method for stable and efficient computation of Green's functions, *Bull. Seismol. Soc. Am.*, *89*(3), 733–7410.
Wang, R., S. Parolai, M. Ge, M. Jin, T. R. Walter, and J. Zschau (2013), The 2011 Mw 9.0 Tohoku earthquake: Comparison of GPS and strong-motion data, *Bull. Seismol. Soc. Am.*, *103*(2B), 1336–1347, doi:10.1785/0120110264.
Wei, S., D. Helmberger, Z. Zhan, and R. Graves (2013), Rupture complexity of the Mw 8.3 sea of okhotsk earthquake: Rapid triggering of complementary earthquakes?, *Geophys. Res. Lett.*, *40*, 5034–5039, doi:10.1002/grl.50977.
Xu, C., Y. Liu, Y. Wen, and R. Wang (2010), Coseismic slip distribution of the 2008 Mw 7.9 Wenchuan earthquake from joint inversion of GPS and InSAR data, *Bull. Seismol. Soc. Am.*, *100*(5B), 2736–2749, doi:10.1785/0120090253.
Xu, L., G. Patau, and Y. Chen (2002), Source time functions of the 1999, Taiwan, Ms 7.6 earthquake retrieved from IRIS and GEOSCOPE long period waveform data using aftershocks as empirical Green's functions, *Acta Seismol. Sin.*, *15*(2), 121–133.
Xu, X. W., X. Z. Wen, G. H. Yu, G. H. Chen, Y. Klinger, J. Hubbard, and J. Shaw (2009), Coseismic reverse- and oblique-slip surface faulting generated by the 2008 Mw7.9 Wenchuan earthquake, China, *Geology*, *37*, 515–518.
Yagi, Y., T. Mikumo, J. Pacheco, and G. Reyes (2004), Source rupture process of the Tecomán, Colima, Mexico earthquake of 22 January 2003, determined by joint inversion of teleseismic body-wave and near-source data, *Bull. Seismol. Soc. Am.*, *94*, 1795–1807.
Yang, Z. X., Y. T. Chen, J. R. Su, T. C. Chen, and P. Wu (2012), The hypocenter and origin time of the Mw7.9 Wenchua earthquake of May 12, 2008, *Acta Seismol. Sin.*, *34*(2), 127–136.
Yao, H., P. Gerstoft, P. M. Shearer, and C. Mecklenbräuker (2011), Compressive sensing of the Tohoku-Oki Mw 9.0 earthquake: Frequency-dependent rupture modes, *Geophys. Res. Lett.*, *38*, L20310, doi:10.1029/2011GL049223.

Yue, H., T. Lay, and K. D. Koper (2012), En échelon and orthogonal fault ruptures of the 11 April 2012 great intraplate earthquakes, *Nature*, *490*, 245–249, doi:10.1038/nature11492.

Zhang, G., M. Vallée, X. Shan, and B. Delouis (2012), Evidence of sudden rupture of a large asperity during the 2008 Mw7.9 Wenchuan earthquake based on strong motion analysis, *Geophys. Res. Lett.*, *39*, L17303, doi:10.1029/2012GL052516.

Zhang, Y., W. P. Feng, L. S. Xu, C. H. Zhou, and Y. T. Chen (2009), Spatio-temporal rupture process of the 2008 great Wenchuan earthquake, *Sci. China Ser. D*, *52*(2), 145–154.

Zhang, Y., L. S. Xu, and Y. T. Chen (2012a), Rupture process of the 2011 Tohoku earthquake from the joint inversion of teleseismic and GPS data, *Earthquake Sci.*, *25*, 129–135, doi:10.1007/s11589-012-0839-1.

Zhang, Y., W. P. Feng, Y. T. Chen, L. S. Xu, Z. H. Li, and D. Forrest (2012b), The 2009 L'Aquila Mw 6.3 earthquake: A new technique to locate the hypocentre in the joint inversion of earthquake rupture process, *Geophys. J. Int.*, *191*, 1417–1426, doi:10.1111/j.1365-246X.2012.05694.x.